
Article:
Hansen, RF, Lewis, TR, Graham, L et al. (2017) OH Production from the Photolysis of Isoprene-derived Peroxy Radicals: Cross-sections, quantum yields and atmospheric implications. Physical Chemistry Chemical Physics, 19 (3). pp. 2332-2345. ISSN: 1463-9076

https://doi.org/10.1039/C6CP06718B

PCCP

Accepted Manuscript

This article can be cited before page numbers have been issued, to do this please use: R. Hansen, T. R. Lewis, L. Graham, L. K. Whalley, P. Seakins, D. E. Heard and M. Blitz, *Phys. Chem. Chem. Phys.*, 2016, DOI: 10.1039/C6CP06718B.

View Article Online
DOI: 10.1039/C6CP06718B

OH Production from the Photolysis of Isoprene-derived Peroxy Radicals: Cross-sections, quantum yields and atmospheric implications

Robert F. Hansen[1], Tom R. Lewis[1], Lee Graham[1], Lisa K. Whalley[1,2], Paul W. Seakins[1,2], Dwayne E. Heard[1,2], Mark A. Blitz[1,2,*]

[1] *School of Chemistry, University of Leeds, Leeds, LS2 9JT, UK*

[2] *National Centre for Atmospheric Science, University of Leeds, Leeds, LS2 9JT, UK*

Abstract

In environments with high concentrations of biogenic volatile organic compounds and low concentrations of nitrogen oxides (NO_x = NO + NO_2), significant discrepancies have been found between measured and modeled concentrations of hydroxyl radical (OH). The photolysis of peroxy radicals from isoprene (HO-Iso-O_2) in the near ultraviolet represents a potential source of OH in these environments, yet has not been considered in atmospheric models. This paper presents measurements of the absorption cross-sections for OH formation ($\sigma_{RO2,OH}$) from the photolysis of HO-Iso-O_2 at wavelengths from 310–362.5 nm via direct observation by laser-induced fluorescence of the additional OH produced following laser photolysis of HO-Iso-O_2. Values of $\sigma_{RO2,OH}$ for HO-Iso-O_2 ranged from $(6.0 \pm 1.6) \times 10^{-20}$ cm^2 $molecule^{-1}$ at 310 nm to $(0.5 \pm 0.15) \times 10^{-20}$ cm^2 $molecule^{-1}$ at 362.5 nm. OH photodissociation yields from HO-Iso-O_2 photolysis, $\phi_{OH,RO2}$, were determined via comparison of the measured values of $\sigma_{RO2,OH}$ to the total absorption cross-sections for HO-Iso-O_2 (σ_{RO2}), which were obtained using a newly-constructed spectrometer. $\phi_{OH,RO2}$ was determined to be 0.13 ± 0.037 at wavelengths from 310–362.5 nm. To determine the impact of HO-Iso-O_2 photolysis on atmospheric OH concentrations, a modeling case-study for a high-isoprene, low-NO_x environment (namely, the 2008 Oxidant and Particle Photochemical Processes above a South-East Asian Tropical Rainforest (OP-3) field campaign, conducted in Borneo) was undertaken using the detailed Master Chemical Mechanism. The model

calculated that the inclusion of HO-Iso-O_2 photolysis in the model had increased the OH concentration by only 1% on average from 10:00–16:00 local time. Thus, HO-Iso-O_2 photolysis alone is insufficient to resolve the discrepancy seen between measured OH concentrations and those predicted by atmospheric chemistry models in such environments.

1. Introduction

Photo-oxidation in the troposphere is a highly complex process and is initiated by short-lived radical species. In the daytime, the dominant radical species is the hydroxyl radical, OH. OH controls the lifetime of the majority of trace gases that are emitted into the atmospheric via anthropogenic or natural processes, for example the greenhouse gas methane. Many of the secondary products produced by atmospheric photo-oxidation of trace gases are harmful to humans and ecosystems. These products include O_3, NO_2, inorganic and organic acids, and multifunctional species. Products of lower volatility partition to the aerosol phase, forming secondary organic aerosol, which can also affect climate and human health. Owing to its short lifetime in the atmosphere, typically less than 1 second, OH is an ideal target for numerical models in order to test the accuracy of embedded chemical mechanisms.[1] The steady-state abundance of atmospheric OH is determined by the balance of its chemical production and loss and does not depend on its transport into and out of the volume being measured. There are now many examples of comparisons between modelled and field measured OH, which are listed in the review by Stone *et al*.[1] There has been relatively good agreement (within model and measurement uncertainties) between modeled and measured OH concentrations in urban environments where ambient mixing ratios of both volatile organic compounds (VOCs) and NO_x are high.[2-5]

However, models have been less successful in calculating OH concentrations, measured either on the ground or from aircraft, in and above low-NO_x environments

View Article Online
DOI: 10.1039/C6CP06718B

influenced by biogenic VOCs.[6-13] Models tend to underpredict OH in these environments, with the level of discrepancy varying from study to study[14], and in general increasing significantly with the concentration of isoprene.[10] Isoprene is a compound of particular importance, as it is emitted by many plant species, and with an emission rate of ~570 Tg yr^{-1}, isoprene represents the largest single emission of a non-methane VOC worldwide.[15, 16] In tropical rainforests, where ambient mixing ratios of isoprene are high (> 1 ppbv) and ambient mixing ratios of NO_x are low (< 1 ppbv), models have underpredicted OH by up to a factor of 10.[8, 12, 13] Tropical rainforests are important examples of high-VOC, low-NO_x environments, as model simulations[17] show that a large fraction of methane can be removed in the lower and free troposphere at tropical latitudes. Enhanced measured-to-modeled OH has also been observed in more anthropogenically influenced environments, such as the Pearl River Delta in China, where there is a biogenic influence from isoprene and ambient mixing ratios of NO_x are low (~0.2 ppbv) at certain times of the day.[10] Hofzumahaus *et al*.[7] show that the modeled OH concentrations can agree with the measured OH concentrations when an additional pathway for the recycling of HO_2 to OH is added to the model. The mechanism for this pathway, however, is still unclear.

A potential explanation for the higher measured than modeled OH levels is the presence of an interference in the OH measurements for environments influenced by biogenic emissions, which were first reported by Mao *et al*. for a laser-induced fluorescence (LIF) instrument[11], and subsequently by Novelli *et al*.[18, 19] The source of this artifically-generated OH, which is thought to originate from the decomposition of species within the sampling assembly/fluorescence cell, is still under investigation[18-20], with the magnitude of the interference from artifically-generated OH likely to vary with instrument design.[1] For the Forschungszentrum Jülich LIF instrument, extensive investigation of potential interferences for the detection of OH did not show any significant interferences for atmospheric

View Article Online
DOI: 10.1039/C6CP06718B

concentrations of reactants during ozonolysis experiments[21], with a similar conclusion reached for the Leeds ground-based instrument, providing evidence that unknown sources of OH production exist in some environments.

In recent years, much effort has gone into the identification of potential sources of this missing OH in low-NO_x environments. Given the dependence of the magnitude of missing OH on isoprene concentrations, it has been suggested that organic peroxy radicals (RO_2) from isoprene (HO-Iso-O_2), which are generated from the reaction of isoprene (C_5H_8) with OH in the presence of O_2,

$$C_5H_8 + OH \xrightarrow{k_1} HO - C_5H_8 \quad \text{(R1)}$$

$$HO - C_5H_8 + O_2 \longrightarrow HO - C_5H_8\,(\text{Iso}) - O_2 \quad \text{(R2)}$$

could be a source of OH.

One potential OH production pathway involves RO_2 reactions that can recycle OH. At low levels of NO_x, removal of RO_2 by reaction with NO is minimal, and the main RO_2 removal mechanism was previously thought to be reaction with HO_2 to form peroxides. Reactions of RO_2 with HO_2 that directly produce OH have been proposed as a source of OH.[9, 22, 23] For example, the reaction of the acetylperoxyl radical ($CH_3C(O)O_2$) with HO_2 has an OH yield of approximately 0.5.[24, 25] Though there is potential for significant OH production through this pathway, it cannot explain the OH in isoprene-rich environments, as the yield of OH for the reaction of isoprene RO_2 with HO_2 has been determined to be less than 0.06.[22] Another suggested pathway consists of consecutive reactions of HO_2 and OH with RO_2 to reform OH and an epoxide.[26] The additional formation of OH, however, is counterbalanced by the loss of OH through reaction with stable products. Therefore, the net OH yield from epoxide formation is small.

Unimolecular reactions of RO_2 comprise a third possible pathway to OH formation from HO-Iso-O_2. Peeters and co-workers[27], using *ab initio* theoretical methods, have

suggested a mechanism (the Leuven Isoprene Mechanism, LIM0) involving isomerization of HO-Iso-O_2 on a fast timescale via H-atom shifts to form a hydroperoxyaldehyde (HPALD), which photolyzes to produce OH. However, Crounse *et al.*[28] measured the bulk isomerization rate of HO-Iso-O_2 to HPALD. The value of the bulk isomerization rate to HPALD that these authors calculated from the parameters of Peeters *et al.*[27] was 50 times less than the measured isomerization rate. In a follow-up study by Wolfe *et al.*[29], a similar C_6 HPALD species was synthesized and photolyzed in an atmospheric chamber, and the OH yield was determined indirectly together with the rate of photolysis of the HPALD. A box model combining the results of these two experiments under atmospheric conditions calculated an increase in [OH] between 5 – 16%; this is too small to explain the higher than modelled OH from field campaigns in forested region.[29] Peeters and co-workers[30] subsequently refined several theoretical parameters, such as barrier heights to RO_2 isomerization, and their new upgraded mechanism LIM1 (Leuven Isoprene Mechanism, v. 1) predicted lower rates of isoprene RO_2 isomerizations, which was consistent with a recent study of isoprene oxidation in the SAPHIR chamber at Forschungszentrum Jülich.[31]

One possibility that has not been greatly explored is the production of OH from the photolysis of organic peroxy radicals (RO_2).

$$RO_2 + h\nu \longrightarrow OH + \text{products} \qquad \text{(R3)}$$

In a modeling study, Frost *et al.*[32] have shown that the near-infrared photolysis of RO_2 to produce OH via the first excited (A) state is thermodynamically accessible. Results of photochemical box model simulations, based on a range of estimated RO_2 absorption cross-sections in the near-infrared and constrained to realistic ambient conditions, suggest that the near-infrared photolysis of RO_2 has the potential to be a significant source of OH in the troposphere. There is experimental evidence of OH production from the ultraviolet photolysis of RO_2 via the second excited (B) state. Kassner *et al.*[33] and Hartmann *et al.*[34]

observed the production of excited-state ($A^2\Sigma^+$) OH from the ultraviolet photolysis of CH_3O_2, but did not quantify the OH that was produced. There is the possibility that other organic peroxy radicals could photolyze to produce OH. Significant (i.e., greater than 10^{-19} cm^2 $molecule^{-1}$) absorption cross-sections have been measured for some organic peroxy radicals at wavelengths above 300 nm. One of these is the acetonylperoxy ($CH_3C(O)CH_2O_2$) radical, which exhibits total absorption cross-sections greater than 5×10^{-19} cm^2 $molecule^{-1}$ above 300 nm.[35, 36] The wavelength region from 300 to 350 nm is of particular importance for RO_2 photolysis in the troposphere, as solar actinic flux in the troposphere is rapidly increasing in this region.[37] However, few measurements of RO_2 total absorption cross-sections and photodissociation quantum yields of OH at wavelengths greater than 300 nm have been reported in the literature.

In this study, we investigate the photolysis of HO-Iso-O_2, focusing on wavelengths above 300 nm. A tunable dye laser was used to photolyze HO-Iso-O_2 at wavelengths from 310 to 362.5 nm. The production of OH was observed from the photolysis of HO-Iso-O_2 at these wavelengths and quantified as absorption cross-sections, weighted to the OH quantum yield. Photodissociation quantum yields of OH were determined through comparison of the absorption cross-section for OH production to the total absorption cross-section for RO_2 measured with a novel multipass absorption apparatus. We investigate the potential impact of OH production from the near-UV photolysis of HO-Iso-O_2 on ambient OH concentrations through a modeling study of the OP-3 campaign in Borneo.

2. Experimental

2.1 RO_2 Photolysis Experiments

The apparatus used for the photolysis experiments is based on the pulsed flash-photolysis/laser-induced fluorescence (PLP-LIF) technique. The design of this apparatus is

View Article Online
DOI: 10.1039/C6CP06718B

similar to one described previously.[38, 39] The main difference is the use of an additional high-energy dye laser to photolyze RO_2 that is typically fired one to two microseconds before the OH probe laser.

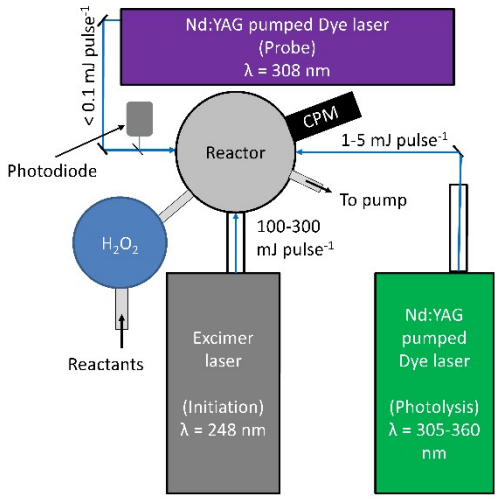

Figure 1. Diagram of the apparatus used for the RO_2 photolysis experiments. The H_2O_2 source (see text) is indicated by the blue circle. CPM stands for channel photomultiplier.

The apparatus used in this study, shown in Figure 1, consisted of a stainless steel reactor (total volume: ~ 1000 cm^3) and three lasers: a high-energy initiation laser (grey) to indirectly generate RO_2, a low-energy probe laser (purple) to probe OH, and a tunable photolysis laser (green) to dissociate the RO_2. The reactor consisted of a 10-way stainless steel cross with four horizontal axes. Reactants were introduced into the reactor through mass flow controllers (MKS Instruments; Brooks Instrument) and entered the reactor via a stainless steel mixing manifold after passing through a bubbler containing H_2O_2. A rotary pump (Edwards RV 5), attached to a port on the reactor, pulled gas through the reactor at a rate of approximately 300 standard cm^3 min^{-1}. The pressure in the reactor (typically ~ 30 Torr) was monitored by a capacitance manometer (MKS Baratron, 0–1000 Torr) attached at the entrance of the reactor. Laser radiation was directed into the reactor through three of the

horizontal axes; a channel photomultiplier (CPM) was located perpendicular to the plane of the laser axes to detect fluorescence.

RO_2 radicals were produced in the reaction cell via the reaction of a target compound with OH. For this study, isoprene and propane were used. Isoprene (Sigma Aldrich, 99.99%) was used without further purification and diluted with nitrogen (BOC, 99.999%), helium (BOC, commercial purity, 99.999%), or argon (BOC, Pureshield, 99.998%), into a 5-L glass bulb. Propane (Air Liquide, 99.9%) was introduced directly from a cylinder without any further purification or dilution. Nitrogen, argon, or helium were added to the reaction mixture to maintain the pressure in the reaction cell at approximately 30–50 Torr. Oxygen (BOC, 99.999%; concentration: 0.5–1 × 10^{17} molecule cm^3) was also added to the reaction mixture to form RO_2 radicals. Hydrogen peroxide (H_2O_2) (Sigma-Aldrich, 50% w/w in H_2O) was used as the OH precursor for these experiments. H_2O_2 can be lost to the walls of the manifold and tubing. Therefore, it was necessary to introduce H_2O_2 by passing the reaction mixture through a bubbler immediately upstream of the reactor (blue circle in Fig. 1) in order to ensure a sufficiently high concentration (on the order of 10^{15} molecule cm^{-3}) of H_2O_2. H_2O_2 was photolyzed using 248 nm radiation from the initiation laser (Lambda Physik LPX 200 Excimer laser operating with KrF, 10 Hz pulse repetition frequency (PRF), energy 50–200 mJ $pulse^{-1}$ cm^{-2}, beam dimensions: 25 mm × 10 mm) to generate OH radicals.

$$H_2O_2 + h\nu \xrightarrow{\lambda = 248\ nm} OH + OH \qquad \text{(R4)}$$

The initial concentrations of OH ranged from 0.1–1 × 10^{14} radicals cm^{-3}.

The target RO_2 was formed via reaction of the OH with the reagent RH (isoprene or propane) in the presence of O_2,

$$OH + RH \xrightarrow{k_5} R + H_2O \qquad \text{(R5)}$$

$$R + O_2 \longrightarrow RO_2 \qquad \text{(R6)}$$

View Article Online
DOI: 10.1039/C6CP06718B

where the concentration of RH was sufficiently high that the predominant reaction of OH was with RH (Reaction R5) and not with H_2O_2 (Reaction R7).

$$OH + H_2O_2 \xrightarrow{k_7} HO_2 + H_2O \qquad \text{(R7)}$$

OH can also be removed through reaction with itself. However, as concentrations of OH in the reactor are approximately 1000 times less than those of H_2O_2, the removal of OH through self-reaction will be much slower than reaction R7.

To determine the relative concentrations of the target reagent and H_2O_2, as well as the timescales for the respective reactions with OH, the pseudo first-order rate constants for the reactions of OH with the chosen reagent and H_2O_2 (k_5[RH] and k_7[H_2O_2], respectively) were measured daily. The values of these rate constants were determined via two-laser flash-photolysis kinetics experiments using only the initiation and probe lasers. In these experiments, the OH loss followed first-order kinetics, as shown by Equation 1,

$$[OH] = [OH]_0 \exp(-k_{obs} t) \qquad (1)$$

where k_{obs} is the observed pseudo first-order rate constant. Experiments were carried out daily in order to determine that the k_{obs} for the target VOC (k_5[RH]) was at least 10 times greater than k_{obs} for H_2O_2 (k_7[H_2O_2]); the timescales of these experiments typically ranged from 50–1000 μs.

Typical values for k_{obs} for reaction R5 under the experimental conditions for this study were greater than 5×10^4 s^{-1} for propane. In the case of isoprene, the measured values of k_{obs} for reaction R5 were greater than 10^5 s^{-1}. The corresponding values of k_{obs} for reaction R7 were typically $1–2 \times 10^4$ s^{-1}. Under these conditions, more than 80% of the OH was converted to RO_2 (90% for isoprene), ensuring that HO_2 production in the reaction cell was minimized.

Once RO_2 was formed in the cell, it was lost slowly (with a lifetime on the order of 10–20 ms). The loss of RO_2 is likely the combination of several loss processes, including the

View Article Online
DOI: 10.1039/C6CP06718B

diffusive loss of the RO_2 from the reaction volume (Reaction R8), the self-reaction of RO_2 (Reaction R9), and the reaction of RO_2 with HO_2 (Reaction R10).

$$RO_2 \longrightarrow \text{loss} \quad \text{(R8)}$$

$$RO_2 + RO_2 \longrightarrow \text{products} \quad \text{(R9)}$$

$$RO_2 + HO_2 \longrightarrow \text{products} \quad \text{(R10)}$$

If some RO_2 were lost via diffusion (reaction R8), a solution to reaction R9 would take this into account. It is noted that even if some HO_2 is produced via reaction R7, as well as other processes (e.g., Reaction R9 or isomerization of HO-Iso-O_2) it will not be an interference in this system. This is because the total absorption cross-sections for HO_2 (σ_{HO2}) are not significant above 300 nm[35, 40]; that is, σ_{HO2} is smaller than 10^{-20} cm^2 molecule^{-1} at 300 nm. Furthermore, no additional OH was observed when the photolysis laser was fired with only H_2O_2 present in the reaction cell.

In these experiments, the delay between the initiation and probe lasers was varied using a custom-built digital timing card, operated by software written in-house using the LabVIEW (National Instruments) environment. By varying the delay between the initiation and probe lasers, the time resolved OH decay could be measured. All timings were referenced to $t = 0$, which coincided with the firing of the initiation laser. To measure the OH generated from photolysis of the H_2O_2 in the absence of RO_2 and to account for background signal from the detector, the probe laser was fired 25–50 times at different delays prior to $t = 0$.

The OH probe laser consisted of a Nd:YAG-pumped (Continuum Precision II) dye laser (Sirah PRSC-DA-24, 10 Hz PRF, energy < 0.1 mJ pulse^{-1}, 3 mm beam diameter, DCM Special). The pulse energy of the probe laser was kept low (< 1 mJ pulse^{-1}, typically ~ 0.1 mJ pulse^{-1}) to minimize additional OH generation from probe-induced photolysis of H_2O_2. To

excite OH, the dye laser was tuned to be on resonance with the $Q_1(2)$ rotational line of the $A^2\Sigma$ ($v' = 0$) ← $X^2\Pi$ ($v'' = 0$) transition of OH at a wavelength of approximately 308 nm. The resulting fluorescence of OH at 308 nm was detected by the CPM; the output was then integrated and recorded by a digital oscilloscope (LeCroy LT 372) and transmitted to a computer for further analysis. For the two-laser kinetics experiments described above, the gain on the CPM was kept low to avoid saturation at early times following the firing of the initiation laser.

Each measurement of the RO_2 absorption cross-section for OH production ($\sigma_{RO2,OH}$), as shown in Figure 2, consisted of a two-laser experiment (black circles) and a three-laser experiment (blue squares), which were conducted back-to-back. In order to observe the OH signal from RO_2 photolysis, which was typically 10–100 times smaller than that from H_2O_2 photolysis, the gain on the CPM was increased. The CPM gain was increased by the same amount for both the two- and three-laser experiments such that both experiments were conducted at the exact same CPM operating conditions. The increased gain led to an overload of the CPM when OH concentrations in the reaction cell were high ($t < 500$ μs). For some experiments where the initiation laser fluence was high (~ 10^{17} photons cm^{-2} $pulse^{-1}$), this overload was especially apparent. It is unclear if this overload was simply a result of the high OH concentration, or if it was related to an overload recovery problem of the CPM. If the former explanation were true, it would be possible to account for this overload by subtraction of the 2-laser OH signal from the 3-laser OH signal. However, the effects of the CPM overload were not reproducible, which tends to suggest that there were overload recovery issues with the CPM. For this reason, and to ensure consistency in the analysis, data points from reaction times less than 500 μs were not included in the analysis for the determination of $\sigma_{RO2,OH}$. Typical timescales for the two-laser and three-laser experiments were 2–5 ms, though some experiments were performed over timescales of 20 ms.

View Article Online
DOI: 10.1039/C6CP06718B

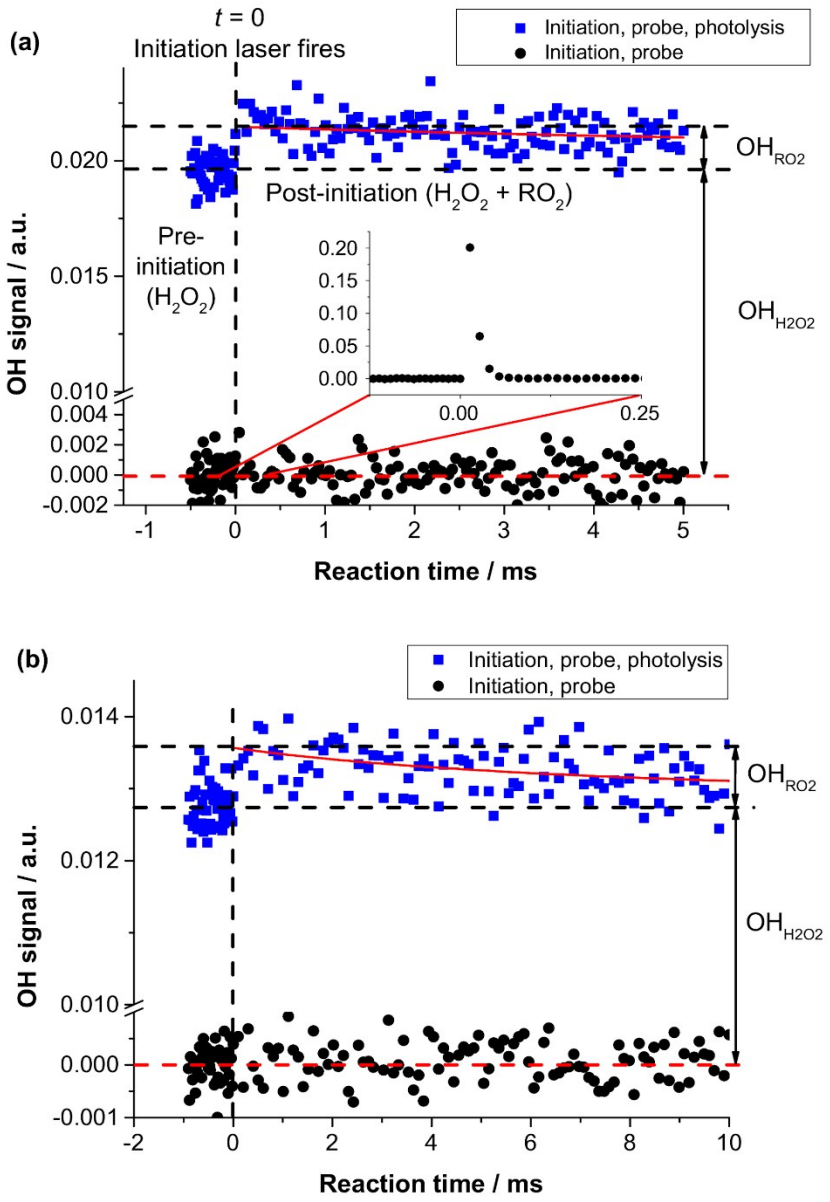

Figure 2. Example of traces from a two-laser (black circles) and a three-laser (blue squares) experiment at photolysis wavelengths of 320 nm (panel a) and 360 nm (panel b) for HO-Iso-O_2. The values of OH_{H2O2} and OH_{RO2} determined from the measured decays are indicated. The fit uses measurements at t > 500 ms. The vertical dashed line is t = 0, where the pre-trigger (t < 0) points, in which only H_2O_2 is present in the reaction volume and able to generate OH, and the post-trigger (t > 0) points, in which both H_2O_2 and RO_2 are present and able to generate OH. The red curves indicate extrapolation of the OH signal (for t > 500 μs)

to $t = 0$, as described in the text. Note the break in the scale of the y-axis. In panel a, a portion of a similar two-laser experiment with a timescale of 2 ms is shown as an inset to demonstrate the timescale of removal of OH by isoprene (see text for details).

For the first of the two experiments, (Fig. 2, black circles), only the initiation and probe lasers were fired. For the second experiment, (Fig. 2, blue squares), the dye laser for RO_2 photolysis was typically fired 1–2 μs before each firing of the probe laser. The photolysis laser was a Nd:YAG-pumped (Litron LPY 664-10) tunable dye laser (Sirah CSTR-G-24, energy 1–10 mJ pulse^{-1}, 10 Hz PRF, 5 mm beam diameter, DCM or pyridine 1) whose output was then doubled by a potassium dihydrogen phosphate (KDP) doubling crystal to generate ultraviolet radiation with wavelengths from 310 – 362.5 nm. This wavelength range was chosen to represent the region where solar actinic flux in the troposphere is rapidly increasing but where there is potentially still significant absorption by RO_2. Given that the rate of OH loss is the same for OH produced by photolysis of H_2O_2 and RO_2, variation of the delay between the photolysis and probe lasers should have no impact on the measured value of $\sigma_{RO2,OH}$. This has been confirmed experimentally with measurements of $\sigma_{RO2,OH}$ made at photolysis-probe delays fixed from 1–10 μs, which showed no significant dependence of $\sigma_{RO2,OH}$ on the magnitude of the delay over this timescale.

For the time points prior to $t = 0$ in the three-laser experiment, the increase in OH signal (relative to the two-laser experiment) represents the OH generated from the photolysis of H_2O_2 by the photolysis laser (i.e., OH_{H2O2}). The increase in OH signal above this baseline after $t = 0$ represents the smaller amounts of OH produced from the photolysis of RO_2 by the photolysis dye laser (i.e., OH_{RO2}). There is the possibility of additional photolysis of the RO_2 from the output of the probe laser. However, the energy of the probe laser (< 1 mJ pulse^{-1}, Fig. 1) is so low in these experiments that photolysis of RO_2 by this laser is minimal. Indeed,

analysis of the two-laser traces in Fig. 2 shows that the OH signal effectively decreases to the pre-trigger baseline by t = 50 μs under typical conditions in this study. The removal of OH via reaction with isoprene can be clearly seen in the inset of Fig. 2a. RO_2 is produced on this timescale; thus, the 2-laser experiment shows that any OH from probe-induced photolysis of RO_2, once RO_2 is generated, is not important. The data for the inset are taken from an experiment conducted on a shorter timescale, as there are more OH measurements at short times (i.e., t < 50 μs). As mentioned previously, the RO_2 generated via Reactions R5 and R6 is gradually removed through self-reaction and pump-out from the reaction volume; this decay of RO_2 can be seen in the OH signal. The OH signal serves as a proxy for RO_2, in this case HO-Iso-O_2. This proxy behavior is evident at long reaction times (t > 0.5 ms), as OH is a product of the photolysis of HO-Iso-O_2. The relationship between the OH signals from photolysis of H_2O_2 (OH_{H2O2}) and RO_2 (OH_{RO2}) is given as Equation 2.

$$\frac{OH_{RO_2}}{OH_{H_2O_2}} = \frac{[RO_2]_0 \times [h\nu]_\lambda \sigma_{RO_2,\lambda}\phi_{RO_2,\lambda}}{[H_2O_2]\times[h\nu]_\lambda \sigma_{H_2O_2,\lambda}\phi_{H_2O_2,\lambda}} = \frac{[h\nu]_{248}[H_2O_2]\sigma_{H_2O_2,248\text{nm}}\phi_{H_2O_2,248\text{nm}} \times [h\nu]_\lambda \sigma_{RO_2,\lambda}\phi_{RO_2,\lambda}}{[H_2O_2]\times[h\nu]_\lambda \sigma_{H_2O_2,\lambda}\phi_{H_2O_2,\lambda}} = \frac{[h\nu]_{248}\sigma_{H_2O_2,248}\sigma_{RO_2,\lambda}\phi_{RO_2,\lambda}}{\sigma_{H_2O_2,\lambda}} \quad (2)$$

It is noted that the initial RO_2 concentration is equal to the initial OH concentration from the photolysis of H_2O_2 by the initiation laser at t = 0, assuming no reaction of OH with H_2O_2. The quantity $[h\nu]_{248}$ represents the fluence (in photons cm^{-2}) of the 248 nm initiation laser, whereas $[h\nu]_\lambda$ represents the fluence of the photolysis laser at the respective wavelength λ. Note that $[h\nu]_\lambda$ is present in the numerator and denominator of Eq. 2, and therefore cancels out of the expression shown in the top line of Eq. 2. The quantity $\sigma_{H2O2,\lambda}$ represents the total absorption cross-section of H_2O_2 at the wavelength λ, and the quantity $\phi_{H2O2,\lambda}$ represents the OH quantum yield from the photolysis of H_2O_2 at the wavelength λ. Likewise, $\sigma_{RO2,\lambda}$ and $\phi_{RO2,\lambda}$ represent the total absorption cross-section and OH quantum yield, respectively, from the photolysis of RO_2 at the wavelength λ. Values for $\sigma_{RO2,\lambda}$ were measured in the absorption

View Article Online
DOI: 10.1039/C6CP06718B

experiments described in Section 2.2. To determine values of σ_{H2O2} for the photolysis wavelengths used for these experiments, the approach described by Kahan *et al.*[41] was used, which incorporates the H_2O_2 total absorption cross-sections recommended by Sander *et al.*[42] A full description of the procedure for the determination of values of $\sigma_{H2O2,\lambda}$ for this study is presented in Section S1 of the Supplement, and the values of σ_{H2O2} used for the determination of $\sigma_{RO2,OH}$ are presented in Table S1. Following the recommendation of Burkholder *et al.*[35], ϕ_{H2O2} is assumed to be 2 for wavelengths greater than 230 nm, which means that $\phi_{H2O2,\,248}$ is equal to $\phi_{H2O2,\,\lambda}$, which leads the ϕ_{H2O2} terms to cancel out in the fractional expression shown in the top line of Eq. 2. Values for $[h\nu]_{248}$ were calculated from measurements of the energy for the initiation laser pulse made with an energy meter (Molectron JMAX 11). These measurements were normalized to the cross-sectional area of the detector head (approximately 1 cm^2) and the measured transmission of the excimer beam through the front window to the center of the reaction cell ($\geq$ 90%). Measurements of the initiation laser energy were performed 2–4 times per day. The initiation laser was aligned such that the center of the beam was located in the center of the reaction cell. The photolysis and probe lasers were also aligned to intersect in the center of the photolysis laser beam. From Table 1, the average uncertainty in the measurements of $\sigma_{RO2,OH}$ is typically 30–40%; this uncertainty is most likely due to the difficulties in aligning the three laser beams rather than inhomogeneities in the initiation laser beam.

The OH produced by the photolysis of the precursor (OH_{H2O2}) over the range 310–362.5 nm was determined by subtraction of the pre-trigger baseline (i.e. the average of the points with $t < 0$) of the three-laser experiment from that of the two-laser experiment (Fig. 2). The OH from RO_2 (OH_{RO2}) was determined by extrapolation of the OH decay after 500 μs back to $t = 0$. The self-reaction of RO_2 (Reaction R9) was assumed to have a greater impact to RO_2 loss than physical removal from the reaction volume. The first-order rate of diffusion

of OH under the conditions of this experiment will typically be less than 50 s^{-1}. A second-order kinetic model (Equation 3), consistent with the self-reaction of RO_2 (Reaction R9) or the reaction of RO_2 with HO_2 (Reaction R10), was fit to this portion of the OH decay for the extrapolation to $t = 0$ (red curve in Fig. 2). The value of $[OH]_0$ is used in Eq. 3 for OH_{RO2}.

$$[OH] = \left(k_{obs} t + \frac{1}{[OH]_0} \right)^{-1} \quad (3)$$

As the removal of RO_2 is slow (RO_2 lifetime > 10–20 ms) compared to the initial removal of OH (which is typically completed by 50 μs), the fit used for extrapolation should not make a significant difference in the determination of $[OH]_0$. The fact that the extrapolations at 320 nm (Fig. 2a) and 360 nm (Fig. 2b) both capture $[OH]_0$ suggests that this method of fitting is robust.

In this way, Equation 2 allowed for the determination of the cross-section for RO_2 photolysis to OH without needing to know the concentration of the RO_2 in the reaction volume.

The quantity $\sigma_{RO2,OH}(\lambda)$, which is defined as the product of $\sigma_{RO2}(\lambda)$ and $\phi_{RO2}(\lambda)$, provides an absolute measure of the OH production from the photolysis of RO_2 and is the quantity obtained from Eq. 1. Values of $\sigma_{RO2,OH}(\lambda)$ are required for calculating the OH production from RO_2 photolysis in an atmospheric model. Rearrangement of Equation 2 yields Equation 4,

$$\sigma_{RO_2,OH}(\lambda) = \sigma_{RO_2}(\lambda)\phi_{OH,RO_2}(\lambda) = \left(\frac{OH_{RO_2}}{OH_{H_2O_2}} \right) \left(\frac{\sigma_{H_2O_2,\lambda}}{\sigma_{H_2O_2,248\text{nm}}} \right) \left(\frac{1}{[h\nu]_{248}} \right) \quad (4)$$

which was used to calculate $\sigma_{RO2,OH}(\lambda)$ from measurements of OH_{RO2} and OH_{H2O2} over the wavelength range considered in this study.

2.2 RO_2 Total Absorption Cross-Section Measurements

View Article Online
DOI: 10.1039/C6CP06718B

Total RO_2 absorption cross-sections (σ_{RO2}) were measured with a multiplexing multipass UV-visible absorption spectrometer incorporating laser flash photolysis. Some details about this apparatus have been provided previously by Lewis *et al.*[43], and a complete description will be provided in a future publication (T. R. Lewis, unpublished work). We provide a brief description of the apparatus and the methodology for determination of RO_2 absorption cross-sections here. The spectrometer consists of a 1.5 m cylindrical reactor maintained at a pressure of 50–350 Torr of nitrogen bath gas for these experiments. The output from a continuous broadband laser-driven light source (Energetiq EQ-99X) was multipassed through the volume of the reactor 13 times. This probe beam was aligned to maximize overlap with the 248 nm output from a KrF excimer laser (Lambda Physik Compex), which was directed through the center of the reaction cell. After passing through the reaction cell, the probe beam was directed through an optical fiber into a spectrograph (Horiba CP140, f/2.5, spectral resolution: 1.5 nm) optimized for the wavelength range of 250–850 nm. This setup permitted the simultaneous measurement of absorption at all wavelengths over this wavelength range. The output from the spectrograph was then measured by a CCD sensor consisting of a 64 × 1044-pixel array (Hamamatsu S7030-1006 FFT). The signals from the CCD sensor were recorded at intervals of 1 ms; each retrieval from the CCD comprised a time point. The data from the CCD sensor were then transferred via a hardware interface to a computer, in which the data were then processed using custom software written in the LabVIEW (National Instruments) environment.

For measurements of σ_{RO2}, RO_2 radicals were generated in the multipass spectrometer by the reaction of a target compound with photolytically-generated OH in the presence of O_2. The target compounds are the same as those used for the measurements of $\sigma_{RO2,OH}$ (Reactions R4-R6). Before the start of each experiment, the absorbance of the H_2O_2 in the reactor was recorded, and from this absorbance measurement, the concentration of H_2O_2 was determined.

The excimer laser (typical energy: 100–150 mJ pulse^{-1}) was fired at a rate of 0.1–0.3 Hz to photolyze H_2O_2 (Sigma-Aldrich, 50% w/w in H_2O), generating OH within the reaction cell (typical OH concentrations: 3–10 × 10^{13} radicals cm^{-3}). This pulse repetition rate was chosen to allow sufficient processing time for the output spectra and to allow the reactor to be replenished, in order to minimize multiple photolysis of the reaction mixture. The OH then reacts with a target compound in the presence of O_2 (typical concentrations: 2–3 × 10^{17} molecules cm^3) to produce the desired RO_2 species within < 100 μs, as for the RO_2 photolysis experiments. The absorption of the broadband light by the RO_2 radicals was measured at 1 ms intervals over the 1-second time period following the excimer laser pulse. Baseline measurements of the intensity of the probe light (I_0) were made before each firing of the excimer laser and consisted of averages of up to 1000 measurements. The custom software processed the CCD sensor data to generate profiles of absorbance as a function of wavelength and time. The traces at each wavelength were extrapolated to determine the absorbance A at t = 0, A_0 (i.e., immediately after firing the excimer laser). The RO_2 concentration was calculated from the OH concentration at t = 0, assuming 1:1 stoichiometry for the reaction of the target compound with OH (Reaction R5). The effective path length (1000 ± 75 cm) of the apparatus was determined experimentally via absorption measurements of NO_2 following the photolysis of a known amount of isopropyl nitrate (i-C_3H_7O–NO_2) with a measured photolysis energy:

$$i\text{-}C_3H_7O - NO_2 + h\nu\,(\lambda = 248\ \text{nm}) \longrightarrow i\text{-}C_3H_7O + NO_2 \qquad \text{(R11)}$$

The NO_2 absorption cross-sections are well known in the literature[44], and the NO_2 yield from R11 has been previously estimated to be unity, based on trends for analogous compounds.[45, 46] The measured fluence $[h\nu]_{248}$ of the 248 nm photolysis laser allows the concentration of NO_2 to be determined via Equation 5:

$$[NO_2] = [i - C_3H_7O - NO_2]\,\sigma_{i-C_3H_7O-NO_2(248\text{nm})}[h\nu]_{248} \qquad (5)$$

View Article Online
DOI: 10.1039/C6CP06718B

The experimentally measured $A_0(\lambda)$ of NO_2 generated photolytically via reaction R11 allowed the effective path length l inside the cell to be determined via the Beer-Lambert expression:

$$l = \frac{A_0(\lambda)}{[NO_2]}\sigma_{NO_2}(\lambda) \quad (6)$$

The uncertainty on the measurement of l, most of which originates from uncertainty on the photolysis laser fluence $[hv]_{248}$ within the reactor, was approximately 14%. The measured absorbance and path length were then used in the Beer-Lambert expression (Eq. 7) to determine σ_{RO2} for each wavelength:

$$A_0(\lambda) = -\ln\left(\frac{I(\lambda)}{I_0(\lambda)}\right) = \sigma_{RO_2}(\lambda)[RO_2]_0 l \quad (7)$$

3. Results and Discussion

3.1 Measurements of $\sigma_{RO2,OH}$

The measurements of $\sigma_{RO2,OH}$ for HO-Iso-O_2 as a function of wavelength are presented in Figure 3 and tabulated in Table 1.

View Article Online
DOI: 10.1039/C6CP06718B

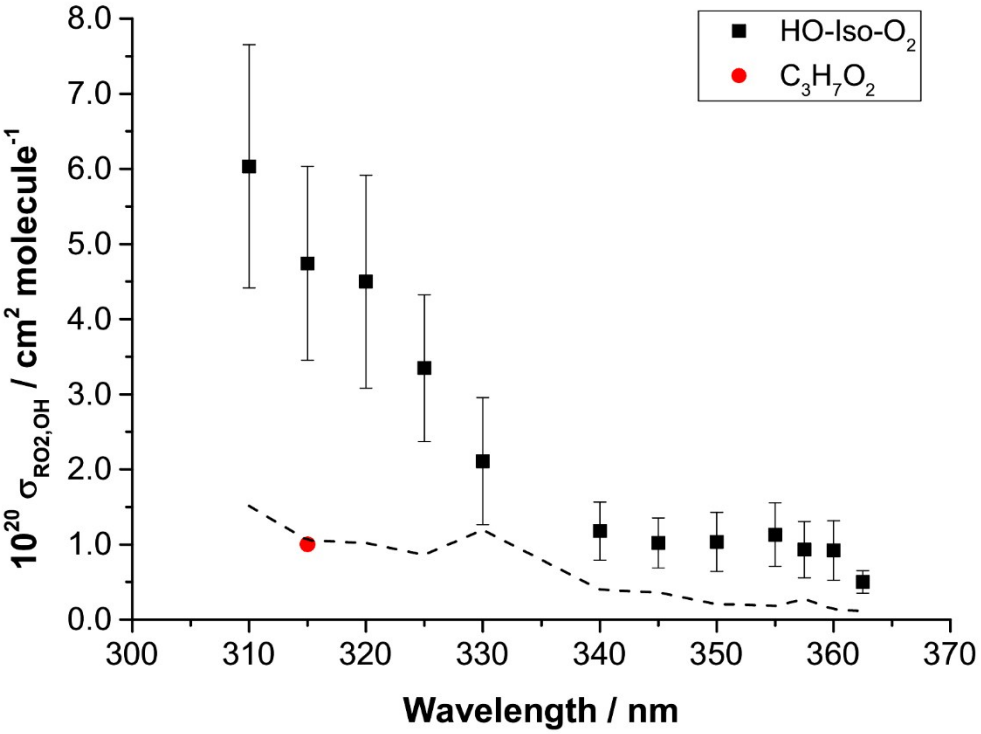

Figure 3. Measurements of $\sigma_{RO2,OH}$, at wavelengths from 310–362.5 nm, for HO-Iso-O_2. Error bars represent the 1σ uncertainty of the datasets at each wavelength for $\sigma_{RO2,OH}$, as described in the text. The estimated upper limit of $\sigma_{RO2,OH}$ for RO_2 derived from propane, which was only determined at 315 nm, is indicated by the red circle. The dashed line indicates the lower limit of $\sigma_{RO2,OH}$ that can be measured with this apparatus, as described in the main text.

As shown in Fig. 3, values of $\sigma_{RO2,OH}$ for HO-Iso-O_2 range from $(6.0 \pm 1.6) \times 10^{-20}$ cm^2 $molecule^{-1}$ at 310 nm to $(0.50 \pm 0.15) \times 10^{-20}$ cm^2 $molecule^{-1}$ at 362.5 nm. The estimated 1σ uncertainty on the measurements of $\sigma_{RO2,OH}$ for HO-Iso-O_2, derived from a propagation of uncertainties on the H_2O_2 cross-sections (estimated at 15%), fits for extrapolations to obtain OH_{RO2}(10–40%), and measurements of initiation laser energy (10%), is approximately 30–40%.

In contrast to HO-Iso-O_2, no significant OH production was seen for RO_2 derived from propane ($C_3H_7O_2$) at 315 nm. Given the absorption spectrum of $C_3H_7O_2$[47, 48], in which the total absorption cross-section steadily decreases at wavelengths above 250 nm, a greater likelihood for photolysis, and consequently OH production, would be expected at shorter wavelengths. As no significant OH production was observed from the photolysis at 315 nm, it was assumed that there would be no OH production from the photolysis of propane RO_2 at wavelengths greater than 315 nm. From the noise (1σ) on the baseline for the three-laser experiments with $C_3H_7O_2$ at 315 nm, an upper limit for $\sigma_{RO2,OH}$ for $C_3H_7O_2$ of 1.0×10^{-20} cm^2 molecule^{-1} is estimated at this wavelength; this is shown as the red circle on Fig. 3.

The lower limit of $\sigma_{RO2,OH}$ that can be measured in this system is when OH_{RO2} is less than or equal to the standard deviation (1σ) in OH_{H2O2}. This means that the lower limit for $\sigma_{RO2,OH}$ is dependent on wavelength and at a single wavelength is dependent on the energy of the excimer laser, which varied between 50 – 200 mJ cm^{-2} pulse^{-1}. There was OH_{H2O2} signal present in all experiments, even at the longest wavelength. The quality of the OH data was to some extent dependent on the bath gas used, so that the limit of $\sigma_{RO2,OH}$ was lower when helium and argon were used as the bath gas. Using typical datasets, we have calculated a lower limit of $\sigma_{RO2,OH}$ as a function of wavelength; this is indicated by the dashed line in Figure 3. The fact that the value of $\sigma_{RO2,OH}$ from the photolysis of $C_3H_7O_2$ is at the lower limit means that it is not significant, and could readily be zero.

The values of $\sigma_{RO2,OH}(\lambda)$ should be independent of the photolysis laser energy, assuming the photolysis of RO_2 is a single-photon process, as $[hv]_\lambda$ cancels in Eq. 1. To test this independence, measurements of $\sigma_{RO2,OH}(\lambda)$ were made at various probe laser energies in the range 1–7 mJ pulse^{-1}. As shown in Figure S2, the values of $\sigma_{RO2,OH}(\lambda)$ measured for RO_2 derived from ethylene show no significant variation (within measurement uncertainty) with

photolysis laser energy. Similarly, there appears to be no significant variation of $\sigma_{RO2,OH}$ with changes in the delay between the photolysis and probe lasers (1–10 μs) or the PRF of the lasers (1–10 Hz).

Total absorption cross-sections for HO-Iso-O_2 (σ_{RO2}) were also measured. Values of σ_{RO2} and $\sigma_{RO2,OH}$ for HO-Iso-O_2 at wavelengths from 300 to 400 nm are plotted in Fig. 4 and tabulated in Table 1.

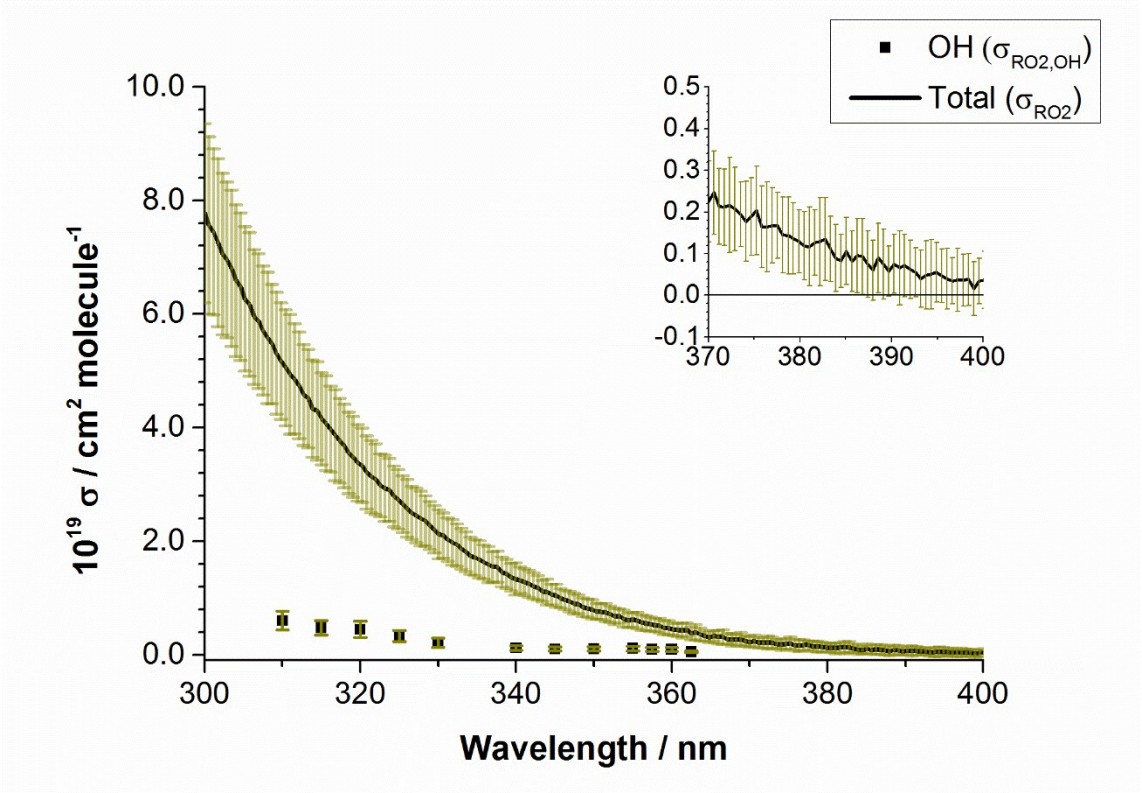

Figure 4. Total absorption cross-sections for HO-Iso-O_2 (σ_{RO2}; black line) and absorption cross-sections for OH production ($\sigma_{RO2,OH}$; black squares) for wavelengths from 300 to 400 nm. The inset shows an expanded view of measurements of σ_{RO2} for wavelengths from 370–400 nm. Error bars represent 1σ precision for σ_{RO2} and the 1σ uncertainty of the data points at each wavelength for $\sigma_{RO2,OH}$.

Table 1. Values of $\sigma_{RO2,OH}$ and σ_{RO2} for HO-Iso-O_2 for each wavelength shown in Fig. 3 and Fig. 4. The stated errors for average $\sigma_{RO2,OH}$ represent 1σ uncertainties for the values at each wavelength; the stated errors for average σ_{RO2} represent the 1σ standard deviation on the calculated values of σ_{RO2} at each wavelength.

Wavelength (nm)	**Average $\sigma_{RO2,OH}$ (10^{-20} cm^2 molecule^{-1})**	**σ_{RO2} (10^{-20} cm^2 molecule^{-1})**		**Number of measurements used to determine average $\sigma_{RO2,OH}$ (N_2, He, Ar)[a]**	**$\phi_{OH,RO2}$**
		Avg ± SD[b]	Fit[c]		
310	6.0 ± 1.62	52 ± 11	52.2	5 (5, 0, 0)	0.12 ± 0.04[d]
315	4.7 ± 1.3	42 ± 8.1	42.2	10 (10, 0, 0)	0.11 ± 0.04
320	4.5 ± 1.4	33 ± 6.5	33.9	39 (36, 0, 3)	0.13 ± 0.05
325	3.4 ± 0.98	26 ± 5.0	27.1	10 (7, 0, 3)	0.12 ± 0.04
330	2.1 ± 0.84	21 ± 4.3	21.4	5 (5, 0, 0)	0.10 ± 0.04
340	1.2 ± 0.39	13 ± 2.8	13.2	4 (0, 4, 0)	0.088 ± 0.03
345	1.0 ± 0.33	10 ± 2.0	10.2	9 (3, 3, 3)	0.10 ± 0.04
350	1.0 ± 0.39	7.6 ± 1.4	7.85	5 (2, 0, 3)	0.14 ± 0.06
355	1.1 ± 0.43	6.2 ± 1.3	5.99	8 (0, 6, 2)	0.18 ± 0.08
357.5	0.93 ± 0.37	5.36± 1.3	5.21	6 (0,3, 3)	0.17 ± 0.08
360	0.92 ± 0.40	4.4 ± 1.0	4.53	4 (0, 0, 4)	0.21 ± 0.1
362.5	0.50 ± 0.15	3.7 ± 1.1	3.92	2 (0, 0, 2)	0.13 ± 0.06

[a]Values in brackets indicate number of points measured in N_2, He, and Ar bath gases, respectively (see text);[b]Average and 1σ standard deviation of 8 individual measurements; [c]Values from fit of a modified Gaussian function (described in Sect. 3.2) to measurements of σ_{RO2};[d]Uncertainty propagated from the errors (1σ) on $\sigma_{RO2,OH}$ and σ_{RO2} stated in this table.

One advantage of the multipass absorption apparatus is its ability to measure, with reasonable accuracy, total absorption cross-sections as low as 10^{-20} cm^2 molecule^{-1} at wavelengths greater than 300 nm. These values are 1–2 orders of magnitude lower than absorption cross-section measurements for organic peroxy radicals reported in the literature. The difficulty of reliably measuring peroxy radical total absorption cross-sections less than 10^{-19} cm^2 molecule^{-1} with traditional absorption measurement techniques may explain the lack of cross-section data for most RO_2 radicals at wavelengths greater than 300 nm. The uncertainty on the measurements of σ_{RO2} is expressed by the errors in Table 2. These

represent the standard deviation (1σ) on the values of σ_{RO2} calculated from Eq. 7. It must be noted that the relative uncertainty on σ_{RO2} increases at wavelengths above than 350 nm due to the increased influence of the noise on the absorption signal, though the relative uncertainty at 362.5 nm is approximately 20%.

The values of σ_{RO2} at 300–310 nm are slightly larger than those reported for other similar alkyl RO_2 species at these wavelengths. The value for σ_{RO2} for HO-Iso-O_2 is $(7.8 \pm 1.6) \times 10^{-19}$ cm^2 molecule^{-1} at 300 nm (Fig. 4), while the corresponding values at 300 nm for other RO_2 are $(4.4 \pm 0.4) \times 10^{-19}$ cm^2 molecule^{-1} for ethylperoxy[49] and $(6.1 \pm 0.6) \times 10^{-19}$ cm^2 molecule^{-1} for vinylperoxy.[50] The total absorption cross-sections for hydroxy-substituted alkylperoxy radicals reported at 300–310 nm are slightly larger than those for the ethylperoxy and vinylperoxy radicals, with values of $(7.7 \pm 0.8) \times 10^{-19}$ cm^2 molecule^{-1} for 2-hydroxyethylperoxy[48] and $(8.0 \pm 1.0) \times 10^{-19}$ cm^2 molecule^{-1} for 2-hydroxy-2-methyl-1-propylperoxy[51] at 300 nm. Given the similarity in functionality between these peroxy radicals and HO-Iso-O_2, it would be expected that the magnitude of the total absorption cross-sections would be similar. The lack of absorption cross-section data for most RO_2 species reported above 300 nm makes it difficult to make more definitive comparisons between the results of this work and values reported in the literature. It must also be noted that, as shown in Fig. 4, the values of σ_{RO2} for HO-Iso-O_2 are consistently higher than those for $\sigma_{RO2,\,OH}$ for HO-Iso-O_2 at all wavelengths considered in this study.

This behavior of $\sigma_{RO2,\,OH}$ relative to σ_{RO2} is reflected in the OH photodissocation quantum yield for RO_2 ($\phi_{OH,RO2}$). To determine $\phi_{OH,RO2}$, the measurements of $\sigma_{RO2,OH}$ were divided by the measurements of the total absorption cross-section (σ_{RO2}) of isoprene RO_2 taken at the same wavelengths as the measurements of $\sigma_{RO2,OH}$.which can be determined by

dividing $\sigma_{RO2,OH}$ by σ_{RO2}, as implied by Equation 4. Values for $\phi_{OH,RO2}$ at wavelengths from 310 to 362.5 nm are plotted in Fig. 5 and tabulated in Table 1.

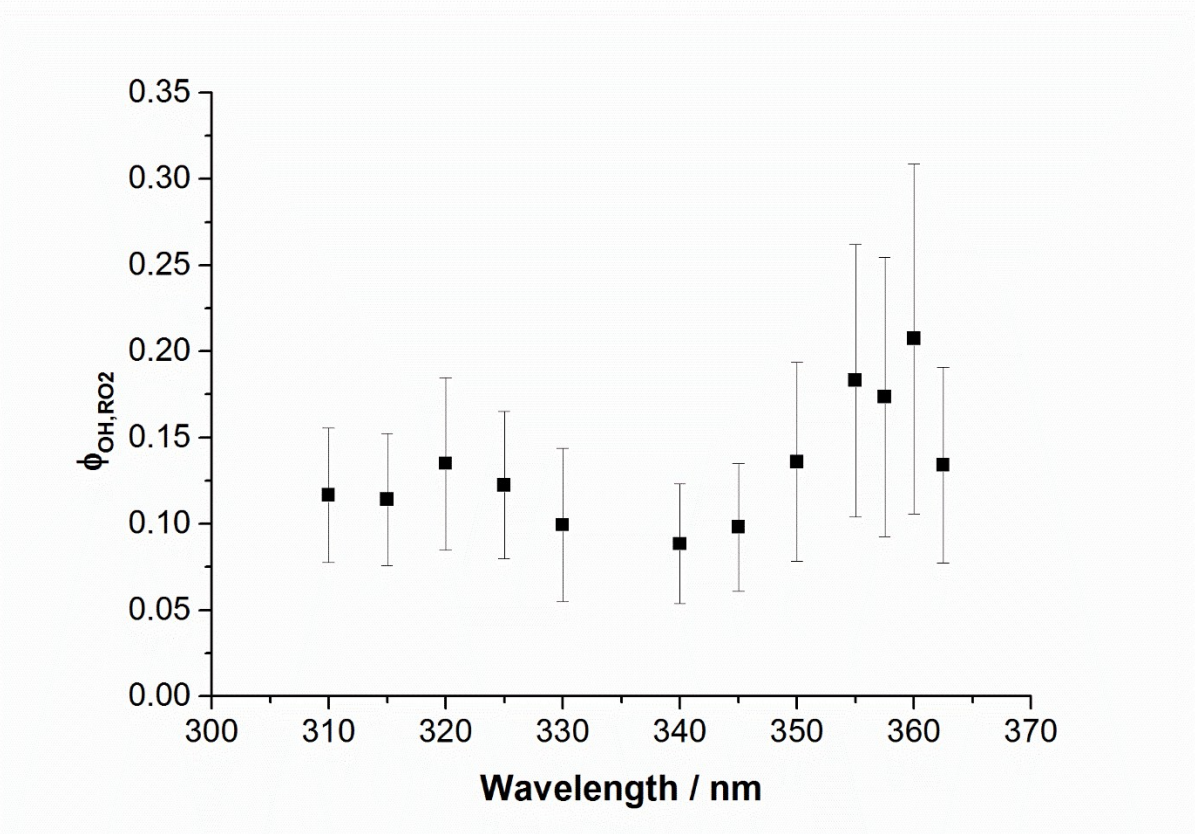

Figure 5. OH yields from isoprene RO_2 photolysis ($\phi_{OH,RO2}$) as a function of wavelength (black squares). Error bars represent the propagation of the 1σ uncertainty of the $\sigma_{RO2,OH}$ measurements at each wavelength and the 1σ standard deviation on the σ_{RO2} measurements at each wavelength.

The value of $\phi_{OH,\,RO2}$ for HO-Iso-O_2 is, on average, 0.13 ± 0.037 at wavelengths from 310 to 362.5 nm (Fig. 5). The OH yield is slightly larger (0.17 to 0.20) at wavelengths from 355 to 360 nm, though this is not significantly different, within uncertainty, to the other values. The finding that the quantum yield is considerably less than unity suggests that other dissociation channels are active in the photolysis of HO-Iso-O_2. The limited time (on the

order of 1–10 μs) between the photolysis and probe pulses suggests that the process which leads to photolytic production of OH must be sufficiently fast to occur on this timescale.

The most likely mechanism for OH formation from the UV photolysis of HO-Iso-O_2 is analogous to the mechanism proposed by Hartmann *et al.*[34] for ground-state OH ($X^2\Pi$) formed from the photolysis of CH_3O_2 at 248 nm. This mechanism consists of two pathways. The first involves the direct photolysis of the O–O bond of HO-Iso-O_2 to produce an alkoxy radical and an O atom:

$$\mathrm{HO-Iso-O_2} \xrightarrow{h\nu} \mathrm{HO-Iso-O} + \mathrm{O(^1D)} \qquad \text{(R12a)}$$

$$\mathrm{HO-Iso-O_2} \xrightarrow{h\nu} \mathrm{HO-Iso-O} + \mathrm{O(^3P)} \qquad \text{(R12b)}$$

The second photolysis channel (Reaction R12) produces OH directly. This channel involves the isomerization of the excited HO-Iso-O_2 to a QOOH species (·Iso-OOH), which then decomposes to form HO-Iso-O and ground-state (OH):

$$\mathrm{HO-Iso-O_2} \xrightarrow{h\nu} \mathrm{HO-Iso-O_2^*} \longrightarrow \mathrm{\cdot Iso-OOH} \longrightarrow \mathrm{HO-Iso-O} + \mathrm{OH}(X\,^2\Pi) \qquad \text{(R12c)}$$

Of the two reactions yielding an oxygen atom (Reactions 12a and 12b), only reaction R12a has a potential pathway to OH formation via secondary reactions: $O(^1D)$ reacts rapidly with VOCs ($k_{O1D+RH} > 10^{-10}$ cm^3 molecule^{-1} s^{-1}; e.g. Blitz *et al.*[52]) to produce OH. To test for the occurrence of this process, $\sigma_{RO2,OH}$ was measured in three different bath gases: nitrogen, helium (BOC, commercial purity, 99.999%), and argon (BOC, Pureshield, 99.998%). The respective bimolecular rate constants of these gases for reaction with $O(^1D)$ are 3.1×10^{-11} cm^3 molecule^{-1} s^{-1}, $< 1 \times 10^{-15}$ cm^3 molecule^{-1} s^{-1}, and $< 8 \times 10^{-13}$ cm^3 molecule^{-1} s^{-1}.[52-55] Thus, if $O(^1D)$ were involved in the production of OH, there would be differences in the values of $\sigma_{RO2,OH}$ for each bath gas. These experiments were conducted at 30–50 Torr, resulting in typical concentrations of N_2, He, Ar of approximately 10^{18} molecule cm^{-3}. At this concentration, $O(^1D)$ has a lifetime ranging from 0.03 μs in nitrogen to 1000 μs in helium.

View Article Online
DOI: 10.1039/C6CP06718B

However, no significant difference, greater than the measurement uncertainty, was observed between values of $\sigma_{RO2,OH}$ for HO-Iso-O_2 measured for all three bath gases, N_2, He and Ar, at 345 nm. The average values of $\sigma_{RO2,OH}$ at 345 nm (± 1σ measurement uncertainty) are $(7.03 \pm 2.3) \times 10^{-21}$ cm^2 molecule^{-1} for N_2, $(11.4 \pm 3.7) \times 10^{-21}$ cm^2 molecule^{-1} for He, and $(12.2 \pm 4.0) \times 10^{-21}$ cm^2 molecule^{-1} for Ar. This independence of $\sigma_{RO2,OH}$ on bath gas suggests that there is no contribution to OH production from the reaction O(^{1}D) with isoprene. This is likely explained by the thermochemistry of Reaction R11a. If the thermochemistry of HO-Iso-O_2 is similar to that of HO_2, i.e., $HO_2 \rightarrow OH + O(^1D)$ has a threshold wavelength of 259 nm[35], then Reaction R11a would not occur above 300 nm. Reaction R11b, however, is a possible channel above 300 nm (with a threshold wavelength of 438 nm[35]), and therefore the formation of O(^{3}P) cannot be ruled out. Photodissociation of HO-Iso-O_2 via Reaction R11b would also yield an alkoxy radical (HO-Iso-O). According to the Master Chemical Mechanism[56], HO-Iso-O decomposes quickly to form stable products (MVK/MACR, HCHO) and HO_2, neither of which would be detected by laser-induced fluorescence at 308 nm. Overall, the observed OH from HO-Iso-O_2 photolysis is consistent with the direct isomerization channel, Reaction R11c.

There is the possibility that the direct isomerization (reaction R12c) produces OH in higher vibrational states (i.e., $v > 0$) due to the excess energy in the UV photons. While we did not attempt to directly detect OH ($v = 1$), if vibrationally-excited OH played a significant role, it would have been detected indirectly by quenching to the ground state by H_2O. H_2O is an efficient quencher of OH ($v = 1$) via reaction R13, with a rate constant[57] of 1.3×10^{-11} cm^3 molecule^{-1} s^{-1}.

$$OH(v=1) + H_2O \longrightarrow OH(v=0) \qquad \text{(R13)}$$

The H_2O_2 solution used in these experiments contains H_2O, and in the gas-phase, concentrations of H_2O are much greater than concentrations of H_2O_2, and it is estimated that in the reactor, the concentration of H_2O is greater than 1×10^{16} molecules cm^{-3}. This translates

to an OH (v = 1) lifetime of approximately 6–7 μs. Therefore, if OH (v = 1) were formed in significant amounts, efficient relaxation by H_2O means that OH (v = 1) should have been detected as OH (v = 0) as the delay between the dye photolysis and probe lasers was increased. As no change in $\sigma_{RO2,OH}$ was observed as the delay time between the photolysis and probe lasers was increased from 1–10 μs, this implies the measured values represent the total amount of OH formed from R12c.

From Figure 5, it can be seen that the OH yield from HO-Iso-O_2 photolysis is low, approximately 10%, on average, at wavelengths from 310–362.5 nm. In the following section, we consider if this low yield is related to the fact that OH arises from the photolysis of specific isomers of HO-Iso-O_2. There are six separate isomers[30, 56] of HO-Iso-O_2, all of which are shown in Figure 6.

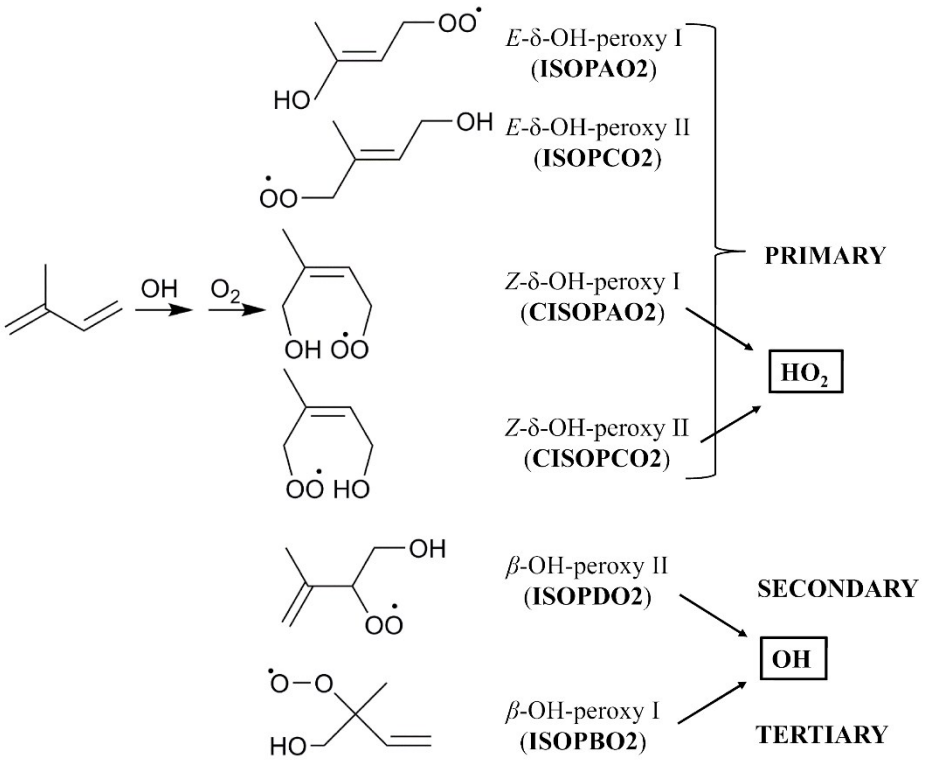

Figure 6. Isomers of HO-Iso-O_2, after Peeters *et al.*[30] The nomenclature in bold type within parentheses corresponds to that used in the MCM v 3.3.1.[56] Isomers are classified according

View Article Online
DOI: 10.1039/C6CP06718B

to the number of atoms β to the carbon atom bonded to the –OO group, as described in the main text. These classifications (PRIMARY, SECONDARY, TERTIARY) are shown on the right-hand side of the figure. In addition, the isomers that produce HO_2 and OH are indicated.

Peeters *et al*.[30] proposed that OH is thermally generated from HO-Iso-O_2 in the ground electronic state through a further isomerization of the *β*-HO-Iso-O_2 isomers that proceeds through a 6-membered transition state, as shown in Fig. 7. This isomerization (also referred to as a 1,5-H shift) produces an hydroperoxy/alkoxy radical, which rapidly decomposes to form OH and stable products, which include formaldehyde and methyl vinyl ketone or methacrolein (depending on the structure of the *β*-HO-Iso-O_2 isomer), as shown in Fig. 7. These thermal OH channels only occur for the secondary and tertiary radicals (shown in Fig. 6). The isomerization scheme in Figure 7 is formally similar to the photolysis scheme given in Reaction R11c.

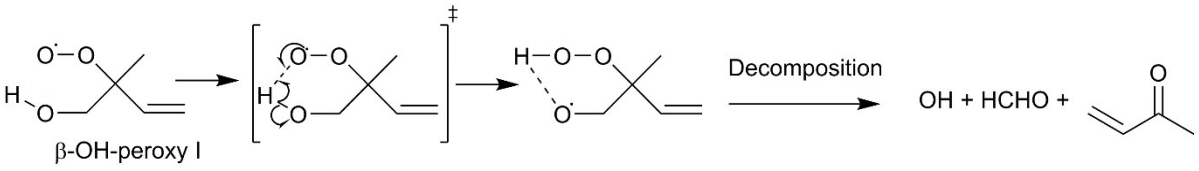

Figure 7. Schematic representation of mechanism proposed by Peeters et al.[27, 30] for the 1,5-shift isomerizations of HO-Iso-O_2 in its ground electronic state. Nomenclature is taken from Peeters *et al*.[30]

If these thermally-active OH channels remain active OH channels upon excitation with UV light, then by looking at the species populations of the isomers, it can be gauged if the production and photodissociation yield of OH is related to a specific isomer. UV radiation with a wavelength of 320 nm corresponds to an energy of 374 kJ mol^{-1}, which is well in excess

View Article Online
DOI: 10.1039/C6CP06718B

of the activation barriers calculated for the 1,5-H shift (88–89 kJ mol^{-1}) isomerization channels by Peeters *et al.*[30] The distribution of the HO-Iso-O_2 isomers can be predicted with the LIM1 mechanism. Model simulations of the OH-isoprene system in Kintecus[58] using the LIM1 mechanism[30] constrained to the conditions of this study, predict distributions of the HO-Iso-O_2 isomer classes that are shown as Figure 8.

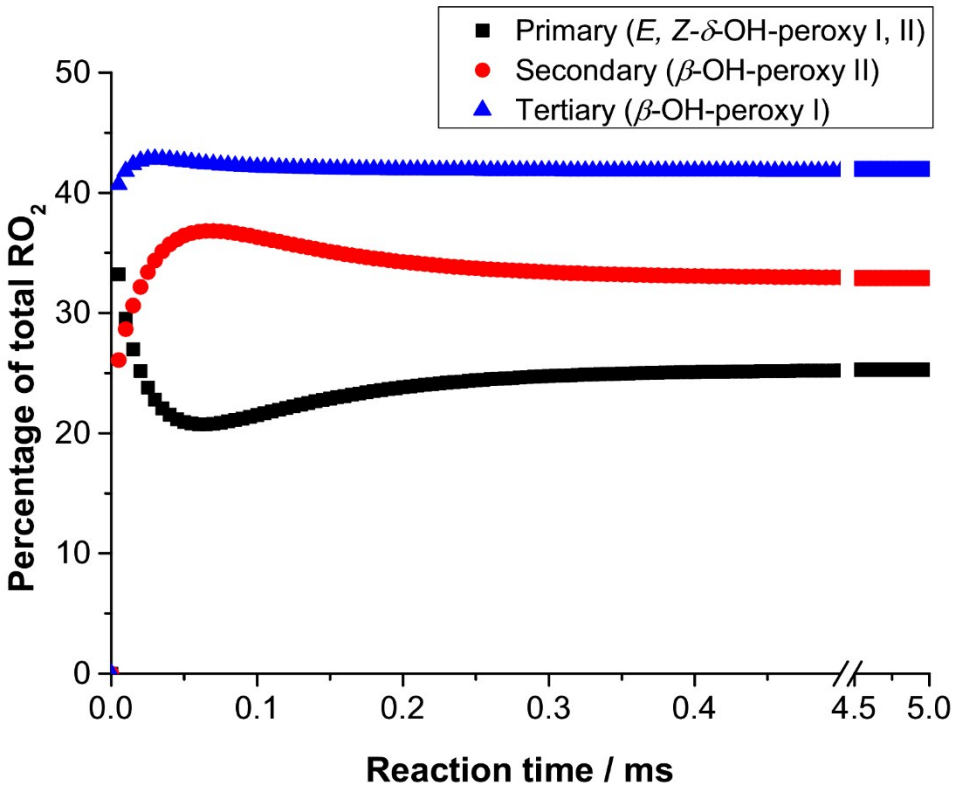

Figure 8. Time evolution of the primary (black squares), secondary (red circles), and tertiary (blue triangles) classes of HO-Iso-O_2 isomers under typical conditions of this study, as predicted by the LIM1[30] mechanism. Nomenclature in the legend follows that of Peeters *et al.*[30] Also note the break in the horizontal axis from 0.5 to 4.5 ms.

Over the timescale of our experiments the isomer distribution remain relatively unchanged where the tertiary and secondary HO-Iso-O_2 are about 70% of the total population. This implies that these isomers do not exclusively produce OH upon UV excitation, hence OH

View Article Online
DOI: 10.1039/C6CP06718B

is only a minor channel and similar to the values given in Figure 5. This conclusion assumes that each isomer is contributing evenly to the absorption spectrum in Figure 4. An examination of the kinetics at different wavelengths, shown in Figure 9, challenges this assumption.

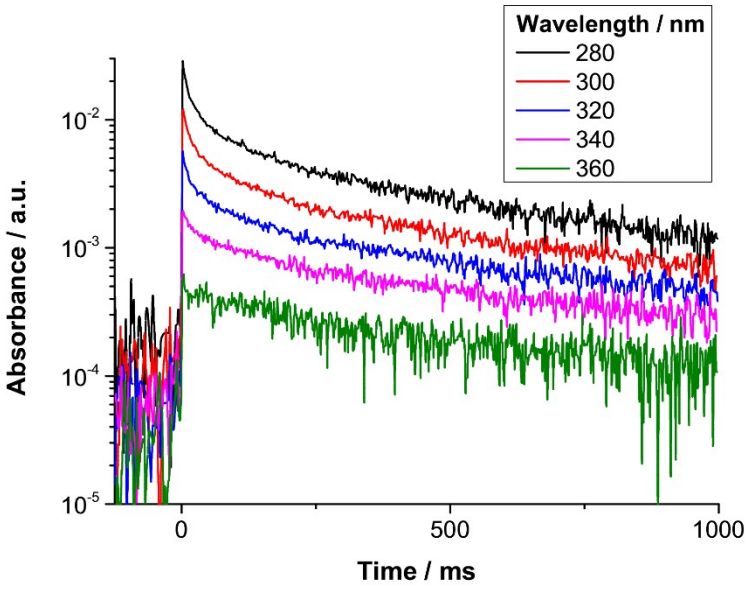

Figure 9. Time-resolved traces of total HO-Iso-O_2 absorption at wavelengths of 280 nm (black), 300 nm (red), 320 nm (blue), 340 nm (magenta), and 360 nm (green), as measured by the multipass absorption apparatus. Note the logarithmic scale on the y-axis.

From Figure 9, it can be observed at 280 nm that there is fast removal, but at the higher wavelengths ($\lambda > 300$ nm), the removal rate is progressively slower, such that by 360 nm there is essentially no significant removal of HO-Iso-O_2. The self-reaction of the tertiary HO-Iso-O_2 radicals is very slow, with a rate constant (derived by Jenkin *et al.*[59]) of 6.9×10^{-14} cm^3 s^{-1}. However, the corresponding rate constants for the self-reaction of the primary and secondary HO-Iso-O_2 radicals are approximately two orders of magnitude faster (~ 4×10^{-12} cm^3 s^{-1}).[59] Therefore, it is clear that at long wavelengths ($\lambda > 340$ nm) the absorption spectrum is mainly from the tertiary HO-Iso-O_2 isomer. More details on the isomer-specific kinetics of HO-Iso-O_2 will be given in a future publication. Overall, an analysis of

RO_2 kinetics as a function of wavelength implies that, at wavelengths greater than 340 nm, all the observed OH is from tertiary HO-Iso-O_2 photolysis, and the photodissociation quantum yield of this tertiary HO-Iso-O_2 isomer is approximately 10%.

The possibility also exists that excited HO-Iso-O_2^*, produced from the interaction of UV photons with HO-Iso-O_2, can be directly quenched via collisions to yield ground-state HO-Iso-O_2. However, the lack of pressure dependence of $\sigma_{OH,RO2}$, between 30–300 Torr, suggests that the direct quenching of HO-Iso-O_2^* is not competitive with dissociation in this system.

There are many possible reasons to explain the small OH yields from HO-Iso-O_2 photolysis. The above argument using the Peeters *et al.*[30] reaction surfaces assumes dissociation on the ground-state when, in fact, the UV light is exciting the RO_2 to its second excited (B) state, from which it may dissociate. Therefore, the mechanism for HO-Iso-O_2 is uncertain. Overall, the production of OH is a minor photodissociation channel for all the isomers, and the major channel is most likely the formation of OH-Iso-O and $O(^3P)$ (Reaction R11b).

3.2 Modeling case study

To assess the impact of the photolysis of HO-Iso-O_2 on modeled OH concentrations, the measurements of $\sigma_{RO2,OH}$ were applied to a field case study of the Oxidant and Photochemical Processes above a Southeast Asian tropical rainforest (OP-3) campaign, which took place at Danum Valley in the Sabah province of Malaysian Borneo.[13] The site at which OH radical concentrations were measured for the OP-3 campaign was dominated by isoprene, which exhibited average daytime mixing ratios of 1–5 ppbv.[13] HO-Iso-O_2 is also the predominant RO_2 species, comprising, at most, approximately half of the total RO_2 concentration for OP-3, as calculated by the model.

For this case study, a zero-dimensional box model was used. This model was based on a subset of the chemistry scheme of the Master Chemical Mechanism (MCM) v. 3.2[60, 61] and constrained to measurements made during the OP-3 campaign. Complete details of the kinetic and photochemical data used in the mechanism are available at the MCM website (http://mcm.leeds.ac.uk/MCM/home). Diurnal average measurements of trace gas concentrations (NO, NO_2, O_3, CO, H_2O, methane, isoprene, α-pinene, limonene, methacrolein, methyl vinyl ketone, ethane, propene, acetylene and C_2-C_6 alkanes), ambient temperature, ambient pressure and $j(O^1D)$ were used to constrain the model. A constant H_2 mixing ratio of 520 pptv was assumed. Values of the model constraints were updated at 15-minute intervals. To prevent the buildup of non-constrained, model-generated species, an additional first-order loss with a rate of 1×10^{-5} s^{-1} was introduced in the model; this is equivalent to a deposition velocity of 1 cm s^{-1} in a 1000 m boundary layer. Photolysis rates, other than $j(O^1D)$, which was measured, were calculated based on a two-stream scattering model[58] that assumes clear-sky conditions. The photolysis rate of RO_2, $j(RO_2)$, was calculated with an actinic flux appropriate for the campaign location and time of year, determined using the TUV model (available at https://www2.acom.ucar.edu/modeling/tropospheric-ultraviolet-and-visible-tuv-radiation-model). This actinic flux (I) was then used with measured values of $\sigma_{RO2,OH}$ to calculate rates for the photolysis for RO_2 yielding OH via Equation 8.

$$j(RO_2) = \int_{\lambda_2}^{\lambda_1} I(\lambda)\sigma_{RO_2}(\lambda)\phi_{OH}(\lambda)\,d\lambda = \int_{\lambda_2}^{\lambda_1} I(\lambda)\sigma_{RO_2,OH}(\lambda)\,d\lambda \qquad (8)$$

As mentioned previously, the quantity $\sigma_{RO2,OH}(\lambda)$ is the product of the total RO_2 absorption cross section $\sigma_{RO2}(\lambda)$ and the quantum yield for OH $\phi_{OH,RO2}(\lambda)$ at the wavelength of interest, and is one of the measured quantities in this work. This makes it possible to use $\sigma_{RO2,OH}(\lambda)$ to directly calculate a rate $j(RO_2)$ for the photolysis of RO_2 yielding OH without the need to know $\sigma_{RO2}(\lambda)$ or $\phi_{OH}(\lambda)$ for the RO_2 species. However, a continuous

representation of $\sigma_{RO2,OH}(\lambda)$ is needed to calculate the photolysis rate for the entirety of the wavelength range of the solar flux, whereas only a subset is measured here. To obtain $\sigma_{RO2}(\lambda)$ as a function of wavelength, a modified Gaussian model, based on a Gram-Charlier series[62] was fit to measurements of $\sigma_{RO2}(\lambda)$. The functional form of the model fit is given as Equation 9, and values of $\sigma_{RO2}(\lambda)$ derived from this fit are included in Table 1.

$$\sigma_{RO_2}(\lambda) = \frac{4.05\times10^{-19}}{(76.8)\times\sqrt{2\pi}} e^{\frac{-z^2}{2}} \left(1+1296.67(z^3-3z)+1330.54(z^4-6z^3+3)\right); \quad z = \frac{\lambda-45.02}{76.8} \tag{9}$$

Values of $\sigma_{RO2}(\lambda)$ determined from Eq. 9 were then multiplied by the average value of $\phi_{OH,RO2}$ from this study to derive values of $\sigma_{RO2,OH}(\lambda)$. This approach takes advantage of the high wavelength resolution of the plot of $\sigma_{RO2}(\lambda)$ as a function of wavelength.

Under cloudy conditions, calculated photolysis rates were scaled to the ratio of observed $j(O^1D)$ to clear-sky (i.e., calculated) $j(O^1D)$. The simultaneous rate equations within the mechanism were solved with the FACSIMILE integrator.[63] The model was allowed to run to steady state (~ 7 days) to allow any unmeasured intermediate species, e.g. unmeasured carbonyls and peroxides, to reach steady state conditions. The OH concentrations from the model were then compared to those measured during the OP-3 campaign. Further details on the modeling for OP-3 are provided by Whalley *et al.*[13]

Two scenarios were considered in this case study. The first scenario was a base case employing chemistry from MCM v. 3.2 and constrained to diurnal averages from the OP-3 campaign, as described above and by Whalley *et al.*[13] In the second scenario (denoted as OHexp), the production OH from the photolysis of HO-Iso-O_2 was added to the base case. Diurnal average photolysis rates for HO-Iso-O_2 were approximately 2×10^{-4} s^{-1} over the time period of 10:00–14:00 LT (local time). Results from both model scenarios are presented in Figure 10.

View Article Online
DOI: 10.1039/C6CP06718B

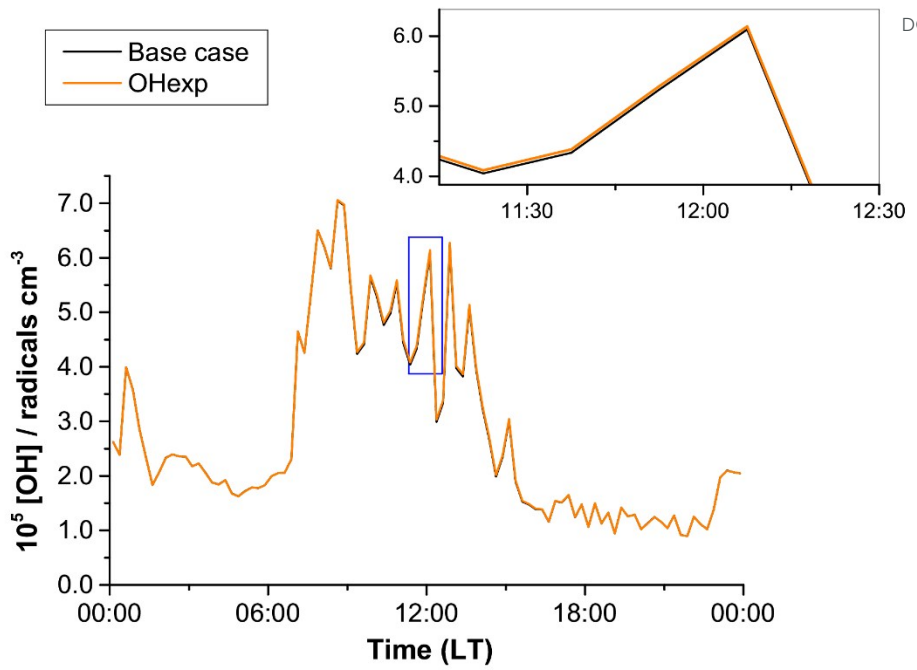

Figure 10. Modeled diurnal average OH concentrations for the base (black) and OHexp (orange) cases, calculated at 15-minute intervals. The inset shows, for clarity, an expanded view of the area contained within the blue box from 11:15–12:30 LT.

The increase in modeled OH concentration from the photolysis of HO-Iso-O_2 is on average 1.0% above the base case averaged between 10:00–16:00 LT. It is noted that only the photolysis of HO-Iso-O_2 was considered in this study, and the photolysis of other RO_2 species may also yield OH. However, as mentioned previously, HO-Iso-O_2 radicals dominated the total daytime concentrations of RO_2 during the OP-3 campaign, accounting for close to half of the total RO_2 predicted around noon local time ([HO-Iso-O_2] = 4.2×10^8 radicals cm^{-3}, total [RO_2] = 1×10^9 radicals cm^{-3}); thus, inclusion of photolysis of other RO_2 species in the model will likely only result in a modest change in [OH] and will not resolve the discrepancy between modelled and observed OH in this environment.

4. Conclusions

Production of OH has been observed from the photolysis of HO-Iso-O_2 in the near ultraviolet at wavelengths from 310–362.5 nm. Production of OH from the photolysis $C_3H_7O_2$ could not be observed at 315 nm. The total absorption cross-sections (σ_{RO2}) and cross-sections for OH production ($\sigma_{RO2,OH}$) for HO-Iso-O_2 are reported for this wavelength range. Values of $\sigma_{RO2,OH}$ for HO-Iso-O_2 range from $6.03 - 0.50 \times 10^{-20}$ cm^2 at wavelengths from 310–362.5 nm, as compared to $74 - 5.3 \times 10^{-20}$ cm^2 for the corresponding σ_{RO2}. OH yields from the photolysis of HO-Iso-O_2, determined from comparison of $\sigma_{RO2,OH}$ and σ_{RO2}, range from 0.08 to 0.15, and are, on average, 0.095 for wavelengths from 310–362.5 nm. It is most likely that $O(^3P)$ + HO-Iso-O is the major channel, as the measured values of $\sigma_{RO2,\ OH}$ are independent of bath gas, ruling out the corresponding $O(^1D)$ channel. Atmospheric box model simulations using the values of $\sigma_{RO2,OH}$ for HO-Iso-O_2 measured in this study have shown that near-UV photolysis of HO-Iso-O_2 is a minor source, 1%, of OH under the ambient conditions encountered during the 2008 OP-3 campaign in Borneo. This increase is far less than that necessary (~ 500–1000%) to match the OH measurements from the OP-3 campaign and is therefore insufficient to explain the ambient OH concentrations measured during this campaign.

Acknowledgements

This work was funded by a grant from the Natural Environment Research Council (NERC, grant NE/K005820/1), and support is also acknowledged from the National Centre for Atmospheric Science, which is funded by NERC.

References

1. D. Stone, L. K. Whalley and D. E. Heard, *Chem. Soc. Rev.*, 2012, **41**, 6348-6404.
2. D. E. Heard, L. J. Carpenter, D. J. Creasey, J. R. Hopkins, J. D. Lee, A. C. Lewis, M. J. Pilling, P. W. Seakins, N. Carslaw and K. M. Emmerson, *Geophys. Res. Lett.*, 2004, **31**.

3. Y. Kanaya, R. Cao, S. Kato, Y. Miyakawa, Y. Kajii, H. Tanimoto, Y. Yokouchi, M. Mochida, K. Kawamura and H. Akimoto, *J. Geophys. Res. [Atmos.]*, 2007, **112**, D11308.
4. D. Mihelcic, F. Holland, A. Hofzumahaus, L. Hoppe, S. Konrad, P. Müsgen, H.-W. Pätz, H.-J. Schäfer, T. Schmitz, A. Volz-Thomas, K. Bächmann, S. Schlomski, U. Platt, A. Geyer, B. Alicke and G. K. Moortgat, *J. Geophys. Res. [Atmos.]*, 2003, **108**, 8254.
5. T. R. Shirley, W. H. Brune, X. Ren, J. Mao, R. Lesher, B. Cardenas, R. Volkamer, L. T. Molina, M. J. Molina, B. Lamb, E. Velasco, T. Jobson and M. Alexander, *Atmos. Chem. Phys.*, 2006, **6**, 2753-2765.
6. N. Carslaw, D. J. Creasey, D. Harrison, D. E. Heard, M. C. Hunter, P. J. Jacobs, M. E. Jenkin, J. D. Lee, A. C. Lewis, M. J. Pilling, S. M. Saunders and P. W. Seakins, *Atmos. Environ.*, 2001, **35**, 4725-4737.
7. A. Hofzumahaus, F. Rohrer, K. Lu, B. Bohn, T. Brauers, C.-C. Chang, H. Fuchs, F. Holland, K. Kita, Y. Kondo, X. Li, S. Lou, M. Shao, L. Zeng, A. Wahner and Y. Zhang, *Science*, 2009, **324**, 1702-1704.
8. D. Kubistin, H. Harder, M. Martinez, M. Rudolf, R. Sander, H. Bozem, G. Eerdekens, H. Fischer, C. Gurk, T. Klüpfel, R. Königstedt, U. Parchatka, C. L. Schiller, A. Stickler, D. Taraborrelli, J. Williams and J. Lelieveld, *Atmos. Chem. Phys.*, 2010, **10**, 9705-9728.
9. J. Lelieveld, T. M. Butler, J. N. Crowley, T. J. Dillon, H. Fischer, L. Ganzeveld, H. Harder, M. G. Lawrence, M. Martinez, D. Taraborrelli and J. Williams, *Nature*, 2008, **452**, 737-740.
10. K. D. Lu, F. Rohrer, F. Holland, H. Fuchs, B. Bohn, T. Brauers, C. C. Chang, R. Haeseler, M. Hu, K. Kita, Y. Kondo, X. Li, S. R. Lou, S. Nehr, M. Shao, L. M. Zeng, A. Wahner, Y. H. Zhang and A. Hofzumahaus, *Atmospheric Chemistry and Physics*, 2012, **12**, 1541-1569.
11. J. Mao, X. Ren, L. Zhang, D. M. Van Duin, R. C. Cohen, J.-H. Park, A. H. Goldstein, F. Paulot, M. R. Beaver, J. D. Crounse, P. O. Wennberg, J. P. DiGangi, S. B. Henry, F. N. Keutsch, C. Park, G. W. Schade, G. M. Wolfe, J. A. Thornton and W. H. Brune, *Atmos. Chem. Phys.*, 2012, **12**, 8009-8020.
12. D. Stone, M. J. Evans, P. M. Edwards, R. Commane, T. Ingham, A. R. Rickard, D. M. Brookes, J. Hopkins, R. J. Leigh, A. C. Lewis, P. S. Monks, D. Oram, C. E. Reeves, D. Stewart and D. E. Heard, *Atmos. Chem. Phys.*, 2011, **11**, 6749-6771.
13. L. K. Whalley, P. M. Edwards, K. L. Furneaux, A. Goddard, T. Ingham, M. J. Evans, D. Stone, J. R. Hopkins, C. E. Jones, A. Karunaharan, J. D. Lee, A. C. Lewis, P. S. Monks, S. J. Moller and D. E. Heard, *Atmos. Chem. Phys.*, 2011, **11**, 7223-7233.
14. F. Rohrer, K. Lu, A. Hofzumahaus, B. Bohn, T. Brauers, C.-C. Chang, H. Fuchs, R. Häeseler, F. Holland, M. Hu, K. Kita, Y. Kondo, X. Li, S. Lou, A. Oebel, M. Shao, L. Zeng, T. Zhu, Y. Zhang and A. Wahner, *Nat. Geosci.*, 2014, **7**, 559-563.
15. A. Guenther, C. N. Hewitt, D. Erickson, R. Fall, C. Geron, T. Graedel, P. Harley, L. Klinger, M. Lerdau, W. A. McKay, T. Pierce, B. Scholes, R. Steinbrecher, R. Tallamraju, J. Taylor and P. Zimmerman, *J. Geophys. Res. [Atmos.]*, 1995, **100**, 8873-8892.
16. A. Guenther, T. Karl, P. Harley, C. Wiedinmeyer, P. I. Palmer and C. Geron, *Atmos. Chem. Phys.*, 2006, **6**, 3181-3210.
17. W. J. Bloss, M. J. Evans, J. D. Lee, R. Sommariva, D. E. Heard and M. J. Pilling, *Faraday Discuss.*, 2005, **130**, 425-436.

18. A. Novelli, K. Hens, C. Tatum Ernest, D. Kubistin, E. Regelin, T. Elste, C. Plass-Dülmer, M. Martinez, J. Lelieveld and H. Harder, *Atmos. Meas. Tech.*, 2014, **7**, 3413-3430.
19. A. Novelli, K. Hens, C. Tatum Ernest, M. Martinez, A. C. Nölscher, V. Sinha, P. Paasonen, T. Petäjä, M. Sipilä, T. Elste, C. Plass-Dülmer, G. J. Phillips, D. Kubistin, J. Williams, L. Vereecken, J. Lelieveld and H. Harder, *Atmos. Chem. Phys. Discuss.*, 2016, DOI: 10.5194/acp-2016-919.
20. A. Novelli, L. Vereecken, J. Lelieveld and H. Harder, *Phys. Chem. Chem. Phys*, 2014, **16**, 19941-19951.
21. H. Fuchs, Z. Tan, A. Hofzumahaus, S. Broch, H.-P. Dorn, F. Holland, C. Künstler, S. Gomm, F. Rohrer, S. Schrade, R. Tillman and A. Wahner, *Atmos. Meas. Tech.*, 2016, **9**, 1431-1447.
22. T. J. Dillon and J. N. Crowley, *Atmos. Chem. Phys.*, 2008, **8**, 4877-4889.
23. J. J. Orlando and G. S. Tyndall, *Chem. Soc. Rev.*, 2012, **41**, 6294-6317.
24. C. B. M. Groß, T. J. Dillon, G. Schuster, J. Lelieveld and J. N. Crowley, *J. Phys. Chem. A*, 2014, **118**, 974-985.
25. F. A. F. Winiberg, T. J. Dillon, S. C. Orr, C. B. M. Groß, I. Bejan, C. A. Brumby, M. J. Evans, S. C. Smith, D. E. Heard and P. W. Seakins, *Atmos. Chem. Phys.*, 2016, **16**, 4023-4042.
26. F. Paulot, J. D. Crounse, H. G. Kjaergaard, A. Kürten, J. M. St. Clair, J. H. Seinfeld and P. O. Wennberg, *Science*, 2009, **325**, 730-733.
27. J. Peeters, T. L. Nguyen and L. Vereecken, *Phys. Chem. Chem. Phys*, 2009, **11**, 5935-5939.
28. J. D. Crounse, F. Paulot, H. G. Kjaergaard and P. O. Wennberg, *Phys. Chem. Chem. Phys.*, 2011, **13**, 13607-13613.
29. G. M. Wolfe, J. D. Crounse, J. D. Parrish, J. M. St. Clair, M. R. Beaver, F. Paulot, T. P. Yoon, P. O. Wennberg and F. N. Keutsch, *Physical Chemistry Chemical Physics*, 2012, **14**, 7276-7286.
30. J. Peeters, J.-F. Müller, T. Stavrakou and V. S. Nguyen, *J. Phys. Chem. A*, 2014, **118**, 8625-8643.
31. H. Fuchs, A. Hofzumahaus, F. Rohrer, B. Bohn, T. Brauers, H.-P. Dorn, R. Haeseler, F. Holland, M. Kaminski, X. Li, K. Lu, S. Nehr, R. Tillman, R. Wegener and A. Wahner, *Nat. Geosci.*, 2013, **6**, 1023-1026.
32. G. J. Frost, G. B. Ellison and V. Vaida, *J. Phys. Chem. A*, 1999, **103**, 10169-10178.
33. C. Kassner, P. Heinrich, F. Stuhl, S. Couris and S. Haritakis, *Chem. Phys. Lett.*, 1993, **208**, 27-31.
34. D. Hartmann, J. Karthäuser and R. Zellner, *J. Phys. Chem.*, 1990, **94**, 2963-2966.
35. J. B. Burkholder, S. P. Sander, J. Abbatt, J. R. Barker, R. E. Huie, C. E. Kolb, M. J. Kurylo, V. L. Orkin, D. M. Wilmouth and P. H. Wine, *Chemical Kinetics and Photochemical Data for Use in Atmospheric Studies, Evaluation No. 18*, Jet Propulsion Laboratory, Pasadena, CA, 2015.
36. R. A. Cox, J. Munk, O. J. Nielsen, P. Pagsberg and E. Ratajczak, *Chem. Phys. Lett.*, 1990, **173**, 206-210.
37. W. B. DeMore, S. P. Sander, D. M. Golden, R. F. Hampson, M. J. Kurylo, C. J. Howard, A. R. Ravishankara, C. E. Kolb and M. J. Molina, *Chemical Kinetics and Photochemical Data for Use in Stratospheric Modeling, Evaluation Number 12*, Report JPL Publication 97-4, Jet Propulsion Laboratory, California Institute of Technology, Pasadena, CA, 1997.
38. L. Onel, M. A. Blitz and P. W. Seakins, *J. Phys. Chem. Lett.*, 2012, **3**, 853-856.

39. L. Onel, L. Thonger, M. A. Blitz, P. W. Seakins, A. J. C. Bunkan, M. Solimannejad and C. J. Nielsen, *J. Phys. Chem. A*, 2013, **117**, 10736-10745.
40. G. S. Tyndall, R. A. Cox, C. Granier, R. Lesclaux, G. K. Moortgat, M. J. Pilling, A. R. Ravishankara and T. J. Wallington, *J. Geophys. Res. [Atmos.]*, 2001, **106**, 12157-12182.
41. T. F. Kahan, R. A. Washenfelder, V. Vaida and S. S. Brown, *J. Phys. Chem. A*, 2012, **116**, 5941-5947.
42. S. P. Sander, J. Abbatt, J. B. Barker, J. B. Burkholder, R. R. Freidl, D. M. Golden, R. E. Huie, C. E. Kolb, M. J. Kurylo, G. K. Moortgat, V. L. Orkin and P. H. Wine, *Chemical Kinetics and Photochemical Data for Use in Atmospheric Studies, Evaluation No. 17*, JPL Publication 10-6, Jet Propulsion Laboratory, Pasadena, CA, 2011.
43. T. R. Lewis, M. A. Blitz, D. E. Heard and P. W. Seakins, *Phys. Chem. Chem. Phys*, 2015, **17**, 4859-4863.
44. A. C. Vandaele, C. Hermans, P. C. Simon, M. Carleer, R. Colin, S. Fally, M. F. Mérienne, A. Jenouvrier and B. Coquart, *J. Quant. Spectrosc. Radiat. Transfer*, 1998, **59**, 171-184.
45. R. Atkinson, D. L. Baulch, R. A. Cox, J. N. Crowley, R. F. Hampson, R. G. Hynes, M. E. Jenkin, M. J. Rossi and J. Troe, *Atmos. Chem. Phys.*, 2006, **6**, 3625-4055.
46. W. T. Luke, R. R. Dickerson and L. J. Nunnermacker, *J. Geophys. Res. [Atmos.]*, 1989, **94**, 14905-14921.
47. H. Adachi and N. Basco, *Int. J. Chem. Kinet.*, 1982, **14**, 1125-1137.
48. P. D. Lightfoot, R. A. Cox, J. N. Crowley, M. Destriau, G. D. Hayman, M. E. Jenkin, G. K. Moortgat and F. Zabel, *Atmos. Environ.*, 1992, **26A**, 1805-1961.
49. M. M. Maricq and T. J. Wallington, *J. Phys. Chem.*, 1992, **96**, 986-992.
50. A. Fahr, A. H. Laufer, M. Krauss and R. Osman, *J. Phys. Chem. A*, 1997, **101**, 4879-4886.
51. S. Langer, E. Ljungström, J. Sehested and O. J. Nielsen, *Chem. Phys. Lett.*, 1994, **226**, 165-170.
52. M. A. Blitz, T. J. Dillon, D. E. Heard, M. J. Pilling and I. D. Trought, *Phys. Chem. Chem. Phys*, 2004, **6**, 2162-2171.
53. E. J. Dunlea and A. R. Ravishankara, *Phys. Chem. Chem. Phys*, 2004, **6**, 2152-2161.
54. A. R. Ravishankara, E. J. Dunlea, M. A. Blitz, T. J. Dillon, D. E. Heard, M. J. Pilling, R. S. Strekowski, J. M. Nicovich and P. H. Wine, *Geophys. Res. Lett.*, 2002, **29**.
55. J. Shi and J. R. Barker, *Int. J. Chem. Kinet.*, 1990, **22**, 1283-1301.
56. M. E. Jenkin, J. C. Young and A. R. Rickard, *Atmos. Chem. Phys. Discuss.*, 2015, **15**, 9709-9766.
57. G. A. Raiche, J. B. Jeffries, K. J. Rensberger and D. R. Crosley, *J. Chem. Phys.*, 1990, **92**, 7258-7263.
58. J. C. Ianni, KINTECUS, Windows Version 2.80, 2002, http://www.kintecus.com.
59. M. E. Jenkin, A. A. Boyd and R. Lesclaux, *J. Atmos. Chem.*, 1998, **29**, 267-298.
60. M. E. Jenkin, S. M. Saunders and M. J. Pilling, *Atmos. Environ.*, 1997, **31**, 81-104.
61. S. M. Saunders, M. E. Jenkin, R. G. Derwent and M. J. Pilling, *Atmos. Chem. Phys.*, 2003, **3**, 161-180.
62. V. B. Di Marco and G. G. Bombi, *J. Chromatogr. A*, 2001, **931**, 1-30.
63. A. R. Curtis and W. P. Sweetenham, *FACSIMILE release H user's manual. AERE Report R11771 (HMSO)*, London, 1987.